

Ångstrom depth resolution with chemical specificity at the liquid-vapor interface

R. Dupuy,^{1,2,*} J. Filser,¹ C. Richter,¹ T. Buttersack,¹ F. Trinter,^{1,3} S. Gholami,¹ R. Seidel,⁴ C. Nicolas,⁵ J. Bozek,⁵ D. Egger,¹ H. Oberhofer,⁶ S. Thürmer,⁷ U. Hergenhahn,¹ K. Reuter,^{1,†} B. Winter,¹ and H. Bluhm^{1,‡}

¹*Fritz-Haber-Institut der Max-Planck-Gesellschaft, Faradayweg 4-6, 14195 Berlin, Germany*

²*Sorbonne Université, CNRS, Laboratoire de Chimie Physique - Matière et Rayonnement, LCPMR, F-75005 Paris Cedex 05, France*

³*Institut für Kernphysik, Goethe-Universität Frankfurt am Main, Max-von-Laue-Str. 1, 60438 Frankfurt am Main, Germany*

⁴*Helmholtz-Zentrum Berlin für Materialien und Energie, Albert-Einstein-Str. 15, 12489 Berlin, Germany*

⁵*Synchrotron SOLEIL, L'Orme des Merisiers, Saint-Aubin - BP 48 91192, Gif-sur-Yvette Cedex, France*

⁶*Department of Physics, University of Bayreuth, 95440 Bayreuth, Germany*

⁷*Department of Chemistry, Graduate School of Science, Kyoto University, Kitashirakawa-Oiwakecho, Sakyo-Ku, Kyoto 606-8502, Japan*

The determination of depth profiles across interfaces is of primary importance in many scientific and technological areas. Photoemission spectroscopy is in principle well suited for this purpose, yet a quantitative implementation for investigations of liquid-vapor interfaces is hindered by the lack of understanding of electron-scattering processes in liquids. Previous studies have shown, however, that core-level photoelectron angular distributions (PADs) are altered by depth-dependent elastic electron scattering and can, thus, reveal information on the depth distribution of species across the interface. Here, we explore this concept further and show that the experimental anisotropy parameter characterizing the PAD scales linearly with the average distance of atoms along the surface normal obtained by molecular dynamics simulations. This behavior can be accounted for in the low-collision-number regime. We also show that results for different atomic species can be compared on the same length scale. We demonstrate that atoms separated by about 1 Å along the surface normal can be clearly distinguished with this method, achieving excellent depth resolution.

Photoemission spectroscopy (PES) has become an important technique for the investigation of liquid-vapor interfaces [1–4], especially since the advent of liquid microjets. PES provides fundamental, molecular-level information on these interfaces. For instance, the electronic energetics of solvated species can be determined [5, 6], allowing for an accurate determination of ionization energies as well as work-function measurements [7–9]. Ultrafast processes, e.g., non-local decay pathways [10] or electron delocalization [11] after excitation were also investigated. Basic yet important questions in chemistry, such as the surface propensity and surface protonation state of solutes can be addressed. More challenging measurements, for instance the investigation of heterogeneous reactions with trace gases are also now becoming possible [12].

An important property of the liquid-vapor interface is the depth distribution and concentration of surfactants and dissolved species in the interfacial region, which can significantly differ from that in the bulk. Depth profiling via PES can be obtained through varying the escape depth of the photoelectrons, either by changing their take-off angle relative to the surface normal (which is only possible under specific experimental conditions, not met, in particular, by cylindrical microjets) or the photoelectron kinetic energy (eKE) by changing the incident photon energy. The eKE influences the inelastic mean free path (IMFP) of the electrons, i.e., the mean distance electrons travel between inelastic-scattering events. Inelastic scattering results in a loss of

kinetic energy of the photoelectrons (in this context a loss of several eV) and hence their removal from the photoelectron signal of interest. The IMFP is, thus, related (in a non-straightforward way) to the escape depth.

The dependence of PE intensities on the escape depth has been widely used in liquid-phase PES [13, 14] to reveal the depth distribution of species at the interface. It has, however, been hampered by several issues. First and foremost, exact values of the IMFP and escape depths in liquid water are still debated [15–19], in particular at low eKE. Even at higher eKE, the uncertainty is still too large to allow for a reliable calculation of depth profiles from PE intensities [1]. Another underexplored quantity is the photoionization cross section of the relevant core levels of the solutes, which relies on calculated atomic data. Ionization cross sections are, for instance, known to exhibit oscillations in molecular, including condensed-phase, systems [20]. For these reasons, obtaining precise and reliable depth profiles from eKE-dependent measurements is often not possible.

Alternative PES-based depth-profiling techniques for the solid state are peak-shape analysis [21] or X-ray standing wave [22] techniques, which are, however, not suitable for liquids and also have their own drawbacks. A few other techniques exist to obtain molecular-scale depth profiles of liquid-vapor interfaces. For example, X-ray reflectivity (XRR) probes the electron density along the surface normal with a resolution down to 3 Å, and when used resonantly can achieve some degree of elemental specificity [23]. Its application to liquid-vapor

interfaces is well established [24]. Another less common technique is neutral-ion backscattering [25], which can similarly achieve a 2–3 Å resolution depth profile, although it requires complex data analysis to extract element-specific profiles. These two techniques nonetheless lack the chemical specificity of PES.

Depth profiling based on photoelectron angular distributions (PADs) from core levels has been explored in a few previous studies [26, 27]. In the condensed phase, the nascent (intrinsic molecular) PAD is modified by elastic electron scattering, which reduces the inherent anisotropy by randomizing the electron trajectories. The PAD for randomly oriented molecules and linearly polarized X-rays is described by [28]

$$\text{PAD}(\theta) \sim 1 + \frac{\beta}{2}(3 \cos^2(\theta) - 1) \quad (1)$$

where θ is the angle between the linear polarization vector of the incident beam and the electron emission direction, and β is the so-called anisotropy parameter, characterizing the angular distribution of photoelectron emission, ranging from $\beta = 2$ to -1 . At the so-called magic angle (54.7°), photoemission becomes independent of β . Elastic electron scattering leads to a reduction of the measured β value as compared to that of the nascent distribution, β_{nascent} . Since the average number of elastic collisions encountered increases with increasing travel distance to the surface, a given reduction in anisotropy can, in principle, be assigned to a given distance to the surface of the point of origin of the photoelectrons.

In this letter, we show how measured PADs can be used to distinguish the average relative depth of atoms within a molecule with a precision of 1 Å. We also show that the relationship between the anisotropy parameter and the probing distance along the surface normal is linear, at least near the interface, and explain this behavior.

Experiments were performed at two different liquid-jet setups installed respectively at the PLEIADES beamline (SOLEIL) and the UE52_SGM beamline (BESSY II) [29]. At both beamlines, the linear polarization vector of the soft X-rays can be freely varied to form an angle between 0° and 90° with respect to the measurement direction, allowing to measure PADs without reorienting the setup, detector, or sample. More experimental details are available in the Supplementary Information (SI) and in previous works [7, 27, 29, 30].

The present study is devoted to perfluorinated pentanoic acid (PFPA) surfactants on an aqueous solution. Perfluorinated surfactants are widely used in industry [31], but are very persistent pollutants and have become a major environmental concern [32]. For our purpose, perfluorinated carboxylic acids possess favorable spectroscopic properties compared to regular hydrogenated molecules. Owing to the large electronegativity of the

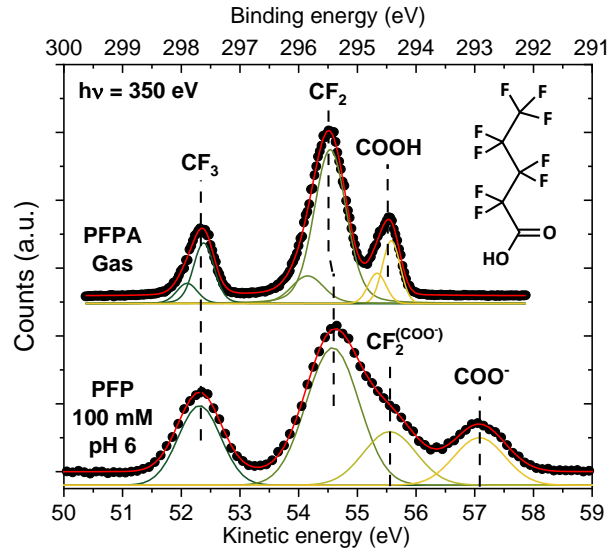


Figure 1. C 1s PE spectra of gaseous perfluorinated pentanoic acid (PFPA) and of an aqueous solution of 100 mM perfluoropentanoate (PFP) at pH 6 measured with a photon energy of 350 eV, corresponding to a kinetic energy of ~ 50 –60 eV, and at the magic angle. Peak assignments are labeled. Both spectra are aligned on the binding-energy axis at the CF_3 peak position; the binding energy axis is not calibrated. Gas-phase peaks were fitted using two Gaussians for each peak, to account for vibrational asymmetry.

fluorine atom, the CF_3 and CF_2 carbons are easily distinguished in PES, and both peaks are also well separated from the COOH carbon peak, as can be seen in the C 1s gas-phase spectrum of PFPA in Fig. 1. This makes it possible to distinguish both ends of the molecule. When in solution, the molecule dissociates (the pK_a is close to 0 [33]) to its deprotonated form (perfluoropentanoate or PFP). PFP exhibits a fourth distinguishable carbon peak in the C 1s PES spectrum (Fig. 1), since the COO^- peak is shifted to lower binding energy compared to COOH , as expected, and a shoulder at the low-binding-energy side of the CF_2 peak can be attributed to the nearest-neighbor CF_2 carbon of the COO^- group. The molecule can, thus, be probed at four different sites along the molecular axis.

We also performed measurements of the O 1s level, where the peak of the oxygen atoms from COO^- can be distinguished from that of liquid and gas-phase water. O 1s spectra together with additional spectra are shown in the SI. Since we expect the surfactant molecules to accumulate at the interface and orient with the hydrophilic COO^- group towards the interface while the hydrophobic perfluorinated tail points towards the vacuum, we are able to probe atoms at different well-defined distances along the surface normal. These assumptions are confirmed with the help of the molecular dynamics (MD) simulations that will be presented below.

First, we need to measure the nascent β_{nascent} of

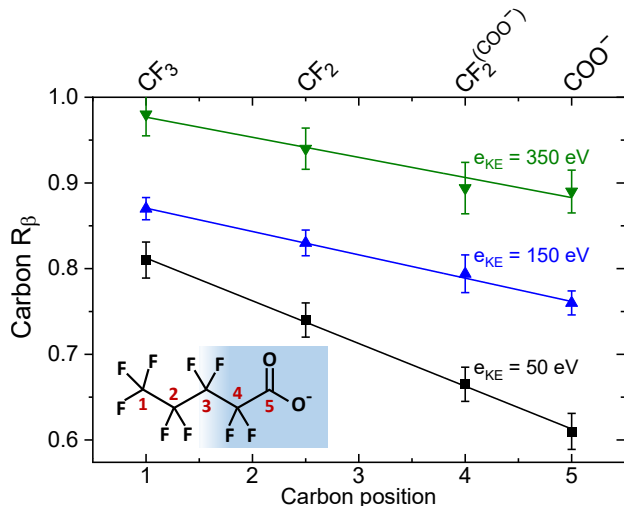


Figure 2. Relative anisotropy parameter R_β of the different carbon sites for a 100 mM PFP solution at pH 6, measured at different eKEs. Results are given for carbon positions 1 to 5 indicated in the structural formula of PFP in the inset, which also shows the expected interface arrangement of the molecule with respect to the water surface. Since carbon 2 and 3 cannot be resolved, the corresponding data point is plotted at position 2.5. A linear trend was fitted to the data.

the molecule in the gas phase, before considering the anisotropy reduction in the condensed phase. For closed, purely atomic core s-orbitals a value of $\beta = 2$ is expected at all eKEs. However, intramolecular scattering and possible changes in orbital character already modify the anisotropy of the PAD of the isolated molecule in the gas phase. To quantify these effects, we performed gas-phase PAD measurements, which we consider to represent the nascent distributions of the liquid-phase molecule. This approximation is discussed in the SI. We have already observed previously [27] that β_{gas} can be different in value for different functional groups of a given molecule. Here, we measured PADs at three different eKEs, 50 eV, 150 eV, and 350 eV. β_{gas} is found to be different for the CF_3 , CF_2 , and COO^- carbons at all eKEs (values are given in the SI), highlighting again the necessity of these gas-phase measurements for proper analysis of liquid-phase results. For the remainder of this letter, we will consider the reduction factor in anisotropy from gas to liquid, $R_\beta = \beta_{liq}/\beta_{gas}$, as the relevant quantity instead of raw β values. For instance, $R_\beta = 0.8$ corresponds to a 20% reduction in anisotropy of the nascent PAD caused by elastic scattering. All measured raw values of β_{gas} and β_{liq} are tabulated in the SI.

R_β values for a 100 mM PFP solution at different eKEs are displayed in Fig. 2. R_β decreases progressively from the CF_3 carbon to the COO^- group carbon, which is the expected behavior for a molecule standing up relative to the surface, with the COO^- group (partly) sol-

vated and the CF_3 pointing towards vacuum. We observe that R_β decreases linearly with carbon position for all eKEs. If we assume equal spacing along the surface normal between all carbons, this means that there is a linear relationship between the average position along the surface normal of the carbon atoms and R_β .

Before addressing this point in more detail, let us further discuss the results of Fig. 2. One can observe that the slope for the eKE = 50 eV data is higher than that for eKE = 150 eV, which in turn is slightly higher than that for eKE = 350 eV. This behavior is indeed qualitatively expected, since the slope should mainly depend on the number of elastic-scattering events per unit of distance, and thus on the inelastic to elastic mean free path ratio, which increases with decreasing eKE.

Another notable finding is the behavior of R_β for the CF_3 group. In the very simple picture sketched in the inset of Fig. 2, it may seem surprising that even the outermost carbon atom experiences scattering (intramolecular scattering being already taken into account by the normalization). However, due to the cylindrical geometry of the jet, the signal is sampled over a wide range of electron take-off angles relative to the surface normal. Furthermore, some disorder is inherent to the liquid surface, where molecules are not necessarily standing straight up and the surface is not atomically flat. Electrons may, thus, scatter on neighboring surfactant molecules even when they originate from the CF_3 group.

To gain more insights into the interface arrangement of the perfluorinated surfactant, we performed MD simulations of NaPFP on a water slab. Details can be found in the SI [34–59]. Vertical distributions of the C and O atoms along the z axis (i.e., the global surface normal) were determined relative to the instantaneous surface of the polar phase [60]. Figure 3(a) displays these distributions, modified by an exponential attenuation factor to account for the fact that the measured signal is exponentially attenuated with depth. We chose an effective attenuation length (EAL) of 12 Å, a reasonable value at 50 eV eKE for water [19], as an approximation. This exponential attenuation does not significantly change the distribution amplitudes as the size of PFP is small compared to the EAL. The non-attenuated distributions are shown in Fig. S5 in the SI.

Figure 3(b) displays the same R_β parameters at the C 1s edge for eKE = 50 eV reported in Fig. 2, but with the x axis now corresponding to the (EAL-modified) average distance relative to the interface derived from Fig. 3(a). The value for the COO^- oxygen atoms from the O 1s data is included as well. The linear decrease of R_β with increasing distance to the interface is confirmed and the R_β value for the COO^- oxygen atoms aligns well with the linear trend for the carbon atoms. Figure 3 demonstrates that PADs of different core levels from different atomic species align on the same scale, and confirms the linear trend for R_β as a function of distance

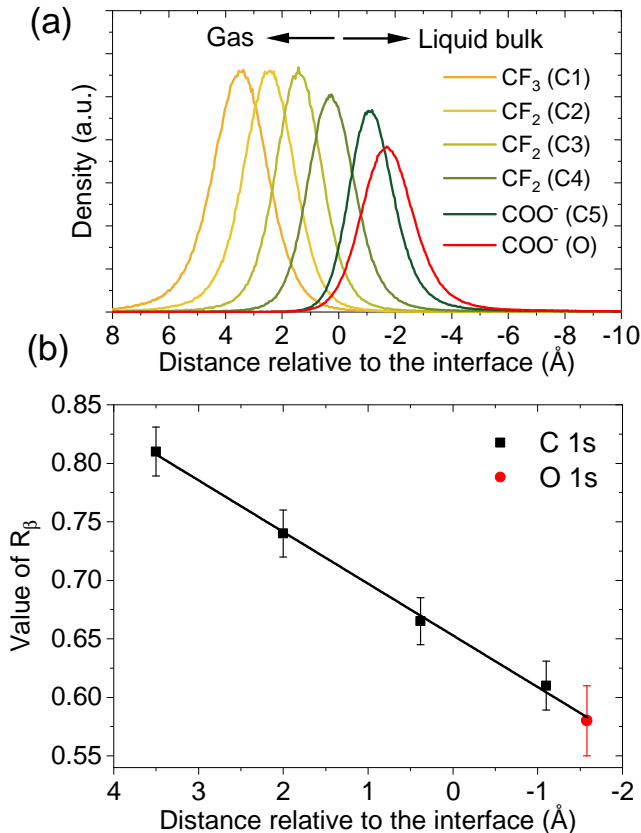


Figure 3. (a) MD-simulations-derived atomic distributions as a function of the distance to the water surface, modified by an exponential attenuation with characteristic length of 12 Å (see the text for details). The position of $z = 0$ is defined in the simulations according to the instantaneous interface (see ref. [61] and SI). (b) Anisotropy parameter R_β (normalized to the gas phase) of the C 1s carbon peaks and COO^- O 1s peak of the PFP molecule, as a function of the average atomic distance to the surface obtained from panel (a).

to the interface.

The sensitivity of the measurement derived from the slope in Fig. 3 is ~ 0.045 per Å. Full error bars, on the other hand, range between 0.04 and 0.06 per Å. Repeated measurements at eKE ~ 150 eV (see Fig. 2) over multiple campaigns were stable within these uncertainties (see SI). The resolution achieved in this experiment is therefore of the order of 1 Å or less under favorable conditions. Indeed, for all (classes of) carbon atoms R_β can be well distinguished above the error bars, and the carbon atoms are separated on average by 1.5 Å along the surface normal.

The sensitivity will vary depending on the details of the PAD measurements, such as the probed core level and the incident photon energy. For instance, the slope of R_β and thus the sensitivity of the measurement depends on eKE (see Fig. 2). Ultimately, it will depend on the elastic-scattering properties of the system. The

achievable sensitivity will also be affected by the precision with which R_β values can be determined.

We now come back to the linearity of the R_β scale and discuss its physical origin. To understand this behavior, we need to consider how the PAD is affected by elastic scattering. The differential cross section (DCS) for elastic scattering, which gives the probability of a deviation from the original trajectory by an angle θ in a single scattering event, is what relates elastic scattering to anisotropy reduction. For an average number of elastic collisions n , Thürmer et al. in their work on the O 1s PADs of liquid water expressed the modified distribution $I^*(\theta)$ as the n -fold convolution of the initial distribution $I(\theta)$ with the DCS: $I^*(\theta) = I(\theta) * (\text{DCS}(\theta))^n$ [19]. This one-dimensional approach ignores specific geometric effects such as the finite angular acceptance of the electron analyzer, but it is sufficient for our purpose. Thürmer et al. showed that the DCS for water can be reasonably approximated by a simple Gaussian of the form $\exp(-\theta^2/2\phi^2)$, with a ‘width’ of $\phi = 17^\circ$, reproducing the measured gas-phase DCS for water satisfactorily. We will adopt the same approximation here, i.e., evaluate the modification of the nascent PAD after n average elastic collisions by calculating the convolution product given above for a Gaussian DCS. One can then deduce the anisotropy parameter β^* of the new distribution as a function of the initial β :

$$\beta^* = \beta \frac{e^{-2n\phi^2}}{1 + \frac{\beta}{4}(1 - e^{-2n\phi^2})} \quad (2)$$

For a low number of collisions ($n \rightarrow 0$), Eq. 2 reduces to:

$$\frac{\beta^*}{\beta} = 1 - (1 + \frac{\beta}{4})2n\phi^2 \quad (3)$$

The difference between the exact formulation (Eq. 2) and a linear approximation (Eq. 3) for $\phi = 17^\circ$ is 2% for $n = 1$, 9% for $n = 2$, and only reaches a significant value of 26% for $n = 3$. Thus, we can consider that for an average number of elastic collisions $n < 2$, β^* scales linearly with n . For an atom located at a specific depth z along the surface normal, n is directly proportional to z . From this simple model, we can account for the observed linear behavior of the measured R_β as a function of z .

While Eqs. 2 and 3 were calculated for the Gaussian approximation of the DCS, they turn out to be valid for other DCS, with only the effective value of ϕ changing. This is discussed in the SI. There are, however, other limitations of this model, such as the fact that the interface exhibits a complex structure with potentially different scattering properties in the surfactant layer below and above the average water level. In fact, one could expect a different behavior above and below

$z = 0$, as atoms are no longer surrounded by water molecules. Above $z = 0$, contributions to scattering only include backscattering on and within the water surface and scattering on other neighboring surfactant molecules. However, as far as can be inferred from the limited number of points and the error bars, no variation in the slope is observed at $z = 0$, which may imply that the scattering properties in water and within the PFP surfactant layer are not sufficiently different to observe a marked change. We note again that the cylindrical geometry of the jet combined with the relative disorder of the surfactant layer likely averages out any specific geometric effect.

While it is not possible to derive quantitative information from the slopes observed in Fig. 2, we can qualitatively account for the observed linear relationship between R_β and the average distance to the interface, which is the important conclusion here. Indeed, at a photoelectron kinetic energy of 50 eV, we can assume an elastic MFP on the order of 5–8 Å for both water and the surfactant, although the exact value is not known. Within the PFP layer, elastic electron scattering should, thus, remain in the single-scattering regime ($n = 1$), where linearity is expected. On the other hand, for electrons experiencing many scattering events, i.e., in case of large elastic-scattering cross sections and/or atoms deep within the interface, the linear relationship should break down.

In conclusion, we have demonstrated a promising depth-profiling technique based on core-level PAD measurements, and made the following observations: (i) The average distance of the origin of a set of photoelectrons to the interface relates linearly with the reduction of its β parameter relative to the gas phase, R_β . (ii) A common R_β scale can be established for all atomic species based on measurements of different core levels. (iii) Å-scale resolution can be achieved, i.e., distinguishable PE peaks originating at an average depth difference of 1 Å can exhibit a difference in R_β exceeding the one-standard-deviation error in this quantity. The sensitivity depends on the experimental conditions.

Compared with other methods mentioned in the introduction of this letter, core-level PAD depth profiling achieves better depth resolution and is not only element-specific but also sensitive to the chemical environment. On the other hand, it only accesses the average depth and not the full depth profile. Nonetheless, our results show that core-level PAD measurements are a powerful tool to study liquid interfaces. The technique should also be applicable to solid-vacuum or solid-vapor interfaces of similarly amorphous systems.

We acknowledge Synchrotron SOLEIL for provision of synchrotron radiation at the PLEIADES beamline, under projects 20201076 and 20211393, and also HZB (Helmholtz-Zentrum Berlin) for the provision of synchrotron radiation at BESSY II, beamline UE52_SGM,

under project 202-09662. We thank the technical service personnel of the SOLEIL chemistry laboratories for their helpful support. R.D. acknowledges support from the Alexander von Humboldt foundation through a Postdoctoral Fellowship. B.W., U.H., and T.B. acknowledge support from the European Research Council (883759-AQUACHIRAL). F.T. and B.W. acknowledge support by the MaxWater initiative of the Max-Planck-Gesellschaft. S.T. acknowledges support from the JSPS KAKENHI Grant No. JP20K15229.

* remi.dupuy@sorbonne-universite.fr

† reuter@fhi.mpg.de

‡ bluhm@fhi.mpg.de

- [1] R. Dupuy, C. Richter, B. Winter, G. Meijer, R. Schlögl, and H. Bluhm, Core level photoelectron spectroscopy of heterogeneous reactions at liquid–vapor interfaces: Current status, challenges, and prospects, *J. Chem. Phys.* **154**, 060901 (2021).
- [2] M. Ammann, L. Artiglia, and T. Bartels-Rausch, X-Ray Excited Electron Spectroscopy to Study Gas–Liquid Interfaces of Atmospheric Relevance, in *Physical Chemistry of Gas-Liquid Interfaces* (Elsevier, 2018) pp. 135–166.
- [3] B. Winter and M. Faubel, Photoemission from Liquid Aqueous Solutions, *Chem. Rev.* **106**, 1176 (2006).
- [4] M. A. Brown, M. Faubel, and B. Winter, X-Ray photo- and resonant Auger-electron spectroscopy studies of liquid water and aqueous solutions, *Annu. Rep. Prog. Chem., Sect. C: Phys. Chem.* **105**, 174 (2009).
- [5] R. Seidel, B. Winter, and S. E. Bradforth, Valence Electronic Structure of Aqueous Solutions: Insights from Photoelectron Spectroscopy, *Annu. Rev. Phys. Chem.* **67**, 283 (2016).
- [6] Y. Tang, H. Shen, K. Sekiguchi, N. Kurahashi, T. Mizuno, Y.-I. Suzuki, and T. Suzuki, Direct measurement of vertical binding energy of a hydrated electron, *Phys. Chem. Chem. Phys.* **12**, 3653 (2010).
- [7] S. Thürmer, S. Malerz, F. Trinter, U. Hergenbahn, C. Lee, D. M. Neumark, G. Meijer, B. Winter, and I. Wilkinson, Accurate vertical ionization energy and work function determinations of liquid water and aqueous solutions, *Chem. Sci.* **12**, 10558 (2021).
- [8] H. Tissot, J.-J. Gallet, F. Bournel, G. Olivieri, M. G. Silly, F. Sirotti, A. Boucly, and F. Rochet, The Electronic Structure of Saturated NaCl and NaI Solutions in Contact with a Gold Substrate, *Top. Catal.* **59**, 605 (2016).
- [9] L. Pérez Ramírez, A. Boucly, F. Saudrais, F. Bournel, J.-J. Gallet, E. Maisonhaute, A. R. Milosavljević, C. Nicolas, and F. Rochet, The Fermi level as an energy reference in liquid jet X-ray photoelectron spectroscopy studies of aqueous solutions, *Phys. Chem. Chem. Phys.* **23**, 16224 (2021).
- [10] T. Jahnke, U. Hergenbahn, B. Winter, R. Dörner, U. Fröhling, P. V. Demekhin, K. Gokhberg, L. S. Cederbaum, A. Ehresmann, A. Knie, and A. Dreuw, Interatomic and Intermolecular Coulombic Decay, *Chem. Rev.* **120**, 11295 (2020).
- [11] D. Nordlund, H. Ogasawara, H. Bluhm, O. Takahashi,

- M. Odellius, M. Nagasono, L. G. M. Pettersson, and A. Nilsson, Probing the Electron Delocalization in Liquid Water and Ice at Attosecond Time Scales, *Phys. Rev. Lett.* **99**, 217406 (2007).
- [12] L. Artiglia, J. Edebeli, F. Orlando, S. Chen, M.-T. Lee, P. Corral Arroyo, A. Gilgen, T. Bartels-Rausch, A. Kleibert, M. Vazdar, M. Andres Carignano, J. S. Francisco, P. B. Shepson, I. Gladich, and M. Ammann, A surface-stabilized ozonide triggers bromide oxidation at the aqueous solution-vapour interface, *Nat. Commun.* **8**, 700 (2017).
- [13] S. Holmberg, R. Moberg, Z. C. Yuan, and H. Siegbahn, Angle resolved electron spectroscopy for measurement of surface segregation phenomena in liquids and solutions, *J. Electron Spectrosc. Relat. Phenom.* **41**, 337 (1986).
- [14] S. Ghosal, J. C. Hemminger, H. Bluhm, B. S. Mun, E. L. D. Hebenstreit, G. Ketteler, D. F. Ogletree, F. G. Requejo, and M. Salmeron, Electron Spectroscopy of Aqueous Solution Interfaces Reveals Surface Enhancement of Halides, *Science* **307**, 563 (2005).
- [15] R. Signorell, Electron Scattering in Liquid Water and Amorphous Ice: A Striking Resemblance, *Phys. Rev. Lett.* **124**, 205501 (2020).
- [16] H. Shinotsuka, B. Da, S. Tanuma, H. Yoshikawa, C. J. Powell, and D. R. Penn, Calculations of electron inelastic mean free paths. XI. Data for liquid water for energies from 50 eV to 30 keV, *Surf. Interface Anal.* **49**, 238 (2017).
- [17] N. Ottosson, M. Faubel, S. E. Bradforth, P. Jungwirth, and B. Winter, Photoelectron spectroscopy of liquid water and aqueous solution: Electron effective attenuation lengths and emission-angle anisotropy, *J. Electron Spectrosc. Relat. Phenom.* **177**, 60 (2010).
- [18] Y.-I. Suzuki, K. Nishizawa, N. Kurahashi, and T. Suzuki, Effective attenuation length of an electron in liquid water between 10 and 600 eV, *Phys. Rev. E* **90**, 010302(R) (2014).
- [19] S. Thürmer, R. Seidel, M. Faubel, W. Eberhardt, J. C. Hemminger, S. E. Bradforth, and B. Winter, Photoelectron Angular Distributions from Liquid Water: Effects of Electron Scattering, *Phys. Rev. Lett.* **111**, 173005 (2013).
- [20] O. Björneholm, J. Werner, N. Ottosson, G. Öhrwall, V. Ekholm, B. Winter, I. Unger, and J. Söderström, Deeper Insight into Depth-Profiling of Aqueous Solutions Using Photoelectron Spectroscopy, *J. Phys. Chem. C* **118**, 29333 (2014).
- [21] S. Tougaard, Energy loss in XPS: Fundamental processes and applications for quantification, non-destructive depth profiling and 3D imaging, *J. Electron Spectrosc. Relat. Phenom.* **178-179**, 128 (2010).
- [22] J. Zegenhagen and A. Kazimirov, *The X-Ray Standing Wave Technique: Principles and Applications*, Series on Synchrotron Radiation Techniques and Applications, Vol. 7 (World Scientific, 2013).
- [23] W. Bu and M. L. Schlossman, Synchrotron X-Ray Scattering from Liquid Surfaces and Interfaces, in *Synchrotron Light Sources and Free-Electron Lasers*, edited by E. J. Jaeschke, S. Khan, J. R. Schneider, and J. B. Hastings (Springer International Publishing, Cham, 2016) pp. 1579–1616.
- [24] M. K. Bera, W. Bu, and A. Uysal, Liquid Surface X-Ray Scattering, in *Physical Chemistry of Gas-Liquid Interfaces* (Elsevier, 2018) pp. 167–194.
- [25] G. Andersson and H. Morgner, Liquid Surfaces, in *Surface and Interface Science*, edited by K. Wandelt (Wiley, 2020) 1st ed., pp. 229–350.
- [26] T. Lewis, B. Winter, S. Thürmer, R. Seidel, A. B. Stephansen, J. A. Freites, D. J. Tobias, and J. C. Hemminger, Molecular Arrangement of a Mixture of Organosulfur Surfactants at the Aqueous Solution–Vapor Interface Studied by Photoelectron Intensity and Angular Distribution Measurements and Molecular Dynamics Simulations, *J. Phys. Chem. C* **123**, 8160 (2019).
- [27] R. Dupuy, J. Filser, C. Richter, R. Seidel, F. Trinter, T. Buttersack, C. Nicolas, J. Bozek, U. Hergenbahn, H. Oberhofer, B. Winter, K. Reuter, and H. Bluhm, Photoelectron angular distributions as sensitive probes of surfactant layer structure at the liquid–vapor interface, *Phys. Chem. Chem. Phys.* **24**, 4796 (2022).
- [28] K. L. Reid, Photoelectron Angular Distributions, *Annu. Rev. Phys. Chem.* **54**, 397 (2003).
- [29] R. Seidel, M. N. Pohl, H. Ali, B. Winter, and E. F. Aziz, Advances in liquid phase soft-x-ray photoemission spectroscopy: A new experimental setup at BESSY II, *Rev. Sci. Instrum.* **88**, 073107 (2017).
- [30] S. Gozem, R. Seidel, U. Hergenbahn, E. Lugovoy, B. Abel, B. Winter, A. I. Krylov, and S. E. Bradforth, Probing the Electronic Structure of Bulk Water at the Molecular Length Scale with Angle-Resolved Photoelectron Spectroscopy, *J. Phys. Chem. Lett.* **11**, 5162 (2020).
- [31] D. M. Lemal, Perspective on Fluorocarbon Chemistry, *J. Org. Chem.* **69**, 1 (2004).
- [32] C. Lau, Perfluorinated Compounds, in *Molecular, Clinical and Environmental Toxicology*, Vol. 3, edited by A. Luch (Springer Basel, Basel, 2012) pp. 47–86, series Title: Experientia Supplementum.
- [33] R. Čabalá, K. Nesměrák, and T. Vlasáková, Dissociation constants of perfluoroalkanoic acids, *Monatsh. Chem.* **148**, 1679 (2017).
- [34] S. Plimpton, Fast Parallel Algorithms for Short-Range Molecular Dynamics, *J. Comput. Phys.* **117**, 1 (1995).
- [35] S. Plimpton, A. Kohlmeyer, A. Thompson, S. Moore, and R. Berger, LAMMPS Stable release 29 September 2021 (stable_29Sep2021_update3). Zenodo. (2020).
- [36] A. P. Thompson, H. M. Aktulga, R. Berger, D. S. Bolintineanu, W. M. Brown, P. S. Crozier, P. J. in 't Veld, A. Kohlmeyer, S. G. Moore, T. D. Nguyen, R. Shan, M. J. Stevens, J. Tranchida, C. Trott, and S. J. Plimpton, LAMMPS - a flexible simulation tool for particle-based materials modeling at the atomic, meso, and continuum scales, *Comput. Phys. Commun.* **271**, 108171 (2022).
- [37] Y. Wu, H. L. Tepper, and G. A. Voth, Flexible simple point-charge water model with improved liquid-state properties, *J. Chem. Phys.* **124**, 024503 (2006).
- [38] W. L. Jorgensen and J. Tirado-Rives, Potential energy functions for atomic-level simulations of water and organic and biomolecular systems, *Proc. Natl. Acad. Sci. U.S.A.* **102**, 6665 (2005).
- [39] L. S. Dodda, I. Cabeza de Vaca, J. Tirado-Rives, and W. L. Jorgensen, LigParGen web server: an automatic OPLS-AA parameter generator for organic ligands, *Nucleic Acids Res.* **45**, W331 (2017).
- [40] A. V. Marenich, S. V. Jerome, C. J. Cramer, and

- D. G. Truhlar, Charge Model 5: An Extension of Hirshfeld Population Analysis for the Accurate Description of Molecular Interactions in Gaseous and Condensed Phases, *J. Chem. Theory Comput.* **8**, 527 (2012).
- [41] P. Melix, patrickmelix/cm5-calculator: First Production Release (v1.0) (2019).
- [42] F. L. Hirshfeld, Bonded-atom fragments for describing molecular charge densities, *Theor. Chim. Acta* **44**, 129 (1977).
- [43] C. Adamo and V. Barone, Toward reliable density functional methods without adjustable parameters: The PBE0 model, *J. Chem. Phys.* **110**, 6158 (1999).
- [44] V. Blum, R. Gehrke, F. Hanke, P. Havu, V. Havu, X. Ren, K. Reuter, and M. Scheffler, Ab initio molecular simulations with numeric atom-centered orbitals, *Comput. Phys. Commun.* **180**, 2175 (2009).
- [45] X. Ren, P. Rinke, V. Blum, J. Wieferink, A. Tkatchenko, A. Sanfilippo, K. Reuter, and M. Scheffler, Resolution-of-identity approach to Hartree-Fock, hybrid density functionals, RPA, MP2 and *GW* with numeric atom-centered orbital basis functions, *New J. Phys.* **14**, 053020 (2012).
- [46] V. W. Yu, F. Corsetti, A. García, W. P. Huhn, M. Jacquelin, W. Jia, B. Lange, L. Lin, J. Lu, W. Mi, A. Seifitokaldani, A. Vázquez-Mayagoitia, C. Yang, H. Yang, and V. Blum, ELSI: A unified software interface for Kohn-Sham electronic structure solvers, *Comput. Phys. Commun.* **222**, 267 (2018).
- [47] V. Havu, V. Blum, P. Havu, and M. Scheffler, Efficient $O(N)$ integration for all-electron electronic structure calculation using numeric basis functions, *J. Comput. Phys.* **228**, 8367 (2009).
- [48] A. C. Ihrig, J. Wieferink, I. Y. Zhang, M. Ropo, X. Ren, P. Rinke, M. Scheffler, and V. Blum, Accurate localized resolution of identity approach for linear-scaling hybrid density functionals and for many-body perturbation theory, *New J. Phys.* **17**, 093020 (2015).
- [49] J. Hermann and A. Tkatchenko, Density Functional Model for van der Waals Interactions: Unifying Many-Body Atomic Approaches with Nonlocal Functionals, *Phys. Rev. Lett.* **124**, 146401 (2020).
- [50] M. M. Reif and P. H. Hünenberger, Computation of methodology-independent single-ion solvation properties from molecular simulations. IV. Optimized Lennard-Jones interaction parameter sets for the alkali and halide ions in water, *J. Chem. Phys.* **134**, 144104 (2011).
- [51] R. W. Hockney and J. W. Eastwood, *Computer Simulation Using Particles* (Routledge; Special Student ed., 1988).
- [52] R. E. Isele-Holder, W. Mitchell, and A. E. Ismail, Development and application of a particle-particle particle-mesh Ewald method for dispersion interactions, *J. Chem. Phys.* **137**, 174107 (2012).
- [53] A. Padua, agiliopadua/ffttool: Update (v1.1). Zenodo. (2019).
- [54] L. Martínez, R. Andrade, E. G. Birgin, and J. M. Martínez, PACKMOL: A package for building initial configurations for molecular dynamics simulations, *J. Comput. Chem.* **30**, 2157 (2009).
- [55] S. Nosé, A unified formulation of the constant temperature molecular dynamics methods, *J. Chem. Phys.* **81**, 511 (1984).
- [56] W. G. Hoover, Canonical dynamics: Equilibrium phase-space distributions, *Phys. Rev. A* **31**, 1695 (1985).
- [57] E. K. Watkins and W. L. Jorgensen, Perfluoroalkanes: Conformational Analysis and Liquid-State Properties from ab Initio and Monte Carlo Calculations, *J. Phys. Chem. A* **105**, 4118 (2001).
- [58] A. H. Larsen, J. J. Mortensen, J. Blomqvist, I. E. Castelli, R. Christensen, M. Dułak, J. Friis, M. N. Groves, B. Hammer, C. Hargus, E. D. Hermes, P. C. Jennings, P. B. Jensen, J. Kermode, J. R. Kitchin, E. L. Kolsbjerg, J. Kubal, K. Kaasbjerg, S. Lysgaard, J. B. Maronsson, T. Maxson, T. Olsen, L. Pastewka, A. Peterson, C. Rostgaard, J. Schiøtz, O. Schütt, M. Strange, K. S. Thygesen, T. Vegge, L. Vilhelmsen, M. Walter, Z. Zeng, and K. W. Jacobsen, The atomic simulation environment—a python library for working with atoms, *J. Phys.: Condens. Matter* **29**, 273002 (2017).
- [59] A. Y. Ng, Feature selection, L1 vs. L2 regularization, and rotational invariance, in *Proceedings of the Twenty-First International Conference on Machine Learning, ICML '04* (Association for Computing Machinery, New York, NY, USA, 2004) p. 78.
- [60] Z. Liu, T. Stecher, H. Oberhofer, K. Reuter, and C. Scheurer, Response properties at the dynamic water/dichloroethane liquid-liquid interface, *Mol. Phys.* **116**, 3409 (2018).
- [61] A. P. Willard and D. Chandler, Instantaneous Liquid Interfaces, *The Journal of Physical Chemistry B* **114**, 1954 (2010).

Supplemental Material to “Ångstrom depth resolution with chemical specificity at the liquid-vapor interface”

R. Dupuy, J. Filser, C. Richter, T. Buttersack, F. Trinter, S. Gholami, R. Seidel, C. Nicolas, J. Bozek, D. Egger, H. Oberhofer, S. Thürmer, U. Hergenbahn, K. Reuter, B. Winter and H. Bluhm

Contents

1	Experimental details and data analysis	2
1.1	Gas-phase measurements	2
1.2	Extraction of β parameters	2
1.3	Gas-phase β values and as-measured liquid β values	4
1.4	Sensitivity limit of the measurements	4
2	Molecular dynamics simulations	5
2.1	Methods	5
2.2	Force-field parameterization	6
2.3	Bias potential	9
3	Validity of the β linearity	10

List of Figures

S1	O 1s gas-phase spectrum of PFPA.	2
S2	Sketch of the experimental geometry.	3
S3	C 1s PADs of 100 mM NaPFP solution.	3
S4	O 1s spectrum and PAD of a NaPFP 100 mM solution.	4
S5	Sample snapshot from MD simulation.	6
S6	Vertical distributions relative to the instantaneous water surface in the MD simulation.	7
S7	Torsional profiles of dihedrals in PFP for which force field parameters were fitted in this work.	8
S8	Biased and unbiased vertical distributions in the MD simulation.	9
S9	Vertical distributions between bulk and surface in the MD simulation.	10
S10	Differential elastic-scattering cross sections and their effect on the anisotropy parameter	11

1 Experimental details and data analysis

1.1 Gas-phase measurements

Gas-phase measurements of photoelectron angular distributions (PADs) were performed to serve as reference for the liquid-phase measurements. As mentioned in the main text, it is important to perform these measurements because we want to extract the reduction of anisotropy of the nascent PAD, i.e., the intrinsic photoemission angular distribution from the condensed-phase molecule, caused by elastic scattering. The nascent PAD in the liquid is assumed to correspond to the gas-phase PAD, which is an approximation, as the molecule is necessarily affected by the aqueous environment. Changes in orbital character or structural changes due to solvation can, in principle, affect the nascent PAD. Since we are probing core levels, orbital or electronic structure changes are considerably reduced as compared to, e.g., shallow valence orbitals. Intramolecular scattering, on the other hand, could conceivably be affected if the molecule undergoes significant conformational changes upon solvation, but we consider this unlikely and will make the hypothesis that this effect can be neglected. The fact that the observed trends are linear at the three eKEs in Fig. 2 of the main text hints at only a small influence of above effects, which would be much more pronounced closer to the threshold.

Gas-phase measurements were performed at the PLEIADES beamline under the same conditions as the liquid-phase measurements. The gas was introduced into the enclosure with the microjet through the catcher aperture, while the jet was not running. The C 1s gas-phase spectrum of PFPA has already been shown in Fig. 1 of the main text. In Fig. S1 we show the O 1s gas-phase spectrum of PFPA. Two distinct bands are observed, originating from a chemical shift of about 2 eV between the C-O-H (lower binding energy) and C=O (higher binding energy) groups.

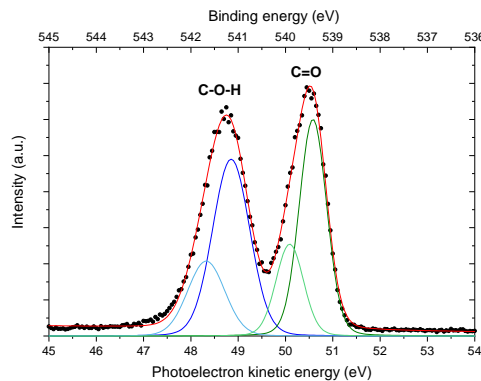


Figure S1: O 1s gas-phase spectrum of PFPA, measured at eKE ~ 50 eV ($h\nu = 590$ eV). Two distinct bands are labeled in the figure. Each band was fitted with two Gaussians to account for peak asymmetry, which do not have any physical meaning.

1.2 Extraction of β parameters

The experimental geometry used for PAD measurements is sketched in fig. S2. PADs were measured by varying the angle of the linear polarization vector of the incident X-ray synchrotron beam with respect to the detection direction, effectively rotating the angular distribution. Spectra were recorded at angles between 0° and 90° . The procedure is similar to that described in previous papers [1, 2, 3].

Stability of the PE (photoelectron) signal is important for a correct assessment of the PAD, and, thus, measurements at 0° were frequently repeated during a measurement series as a stability check. Signal intensities are subsequently corrected for slight photon-flux variations at different polarization angles, which were measured using either a standard AXUV photodiode (at the PLEIADES beamline) or the mirror current on the first mirror (at the UE52_SGM beamline). These normalized intensities as a function of polarization angle are then fitted with the following formula:

$$f(\theta) = A \left(1 + \frac{\beta}{2} (3\cos^2(\theta + \theta_0) - 1) \right) \quad (1)$$

This equation is similar to Eq. 1 in the main text, except it includes a scaling term A and an offset term θ_0 which accounts for a possible slight tilt of the apparatus, vertical beam misalignment, and a systematic difference between

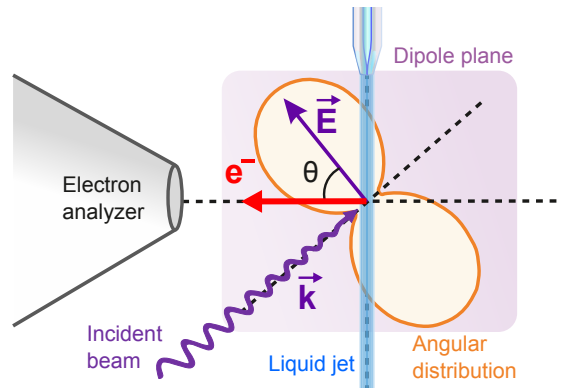


Figure S2: Sketch of the experimental geometry. The light propagation vector \vec{k} , detection direction, and liquid-jet propagation direction are all orthogonal, *i.e.*, the latter two comprise the dipole plane, defined as orthogonal to the light propagation direction. The direction of the light polarization vector \vec{E} can be varied within the dipole plane between 0 and 90° with respect to the detection direction.

the nominal and actual polarization direction, e.g., due to a misalignment of the elliptically polarized undulator). In using Eq. (1), we assume that the synchrotron radiation is perfectly linearly polarized at any angle. An example of measured PADs is given in Fig. S3, with each panel corresponding to one distinguishable carbon peak of a 100 mM NaPFP solution measured at eKE \sim 150 eV. The PADs were then fitted with Eq. (1).

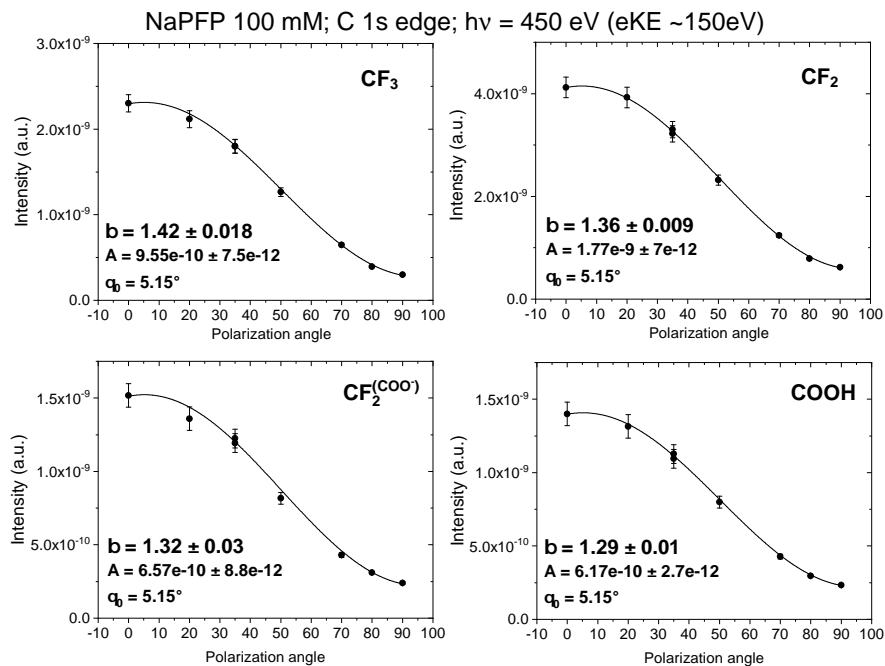


Figure S3: Measured photoelectron angular distributions (PADs) of the different distinguishable C 1s carbon peaks of a 100 mM NaPFP solution, at $h\nu = 450$ eV corresponding to eKE \sim 150 eV. The PADs were fitted with Eq. (1), yielding the parameters indicated in each panel.

In the main text, in addition to the C 1s data, we also present R_β values extracted from a measurement of the

O 1s band. In Fig. S4, we show the O 1s spectrum for the same 100 mM NaPFP solution and the extracted PAD. The spectrum was acquired in the same conditions as the C 1s spectrum of Fig. 1 of the main text, e.g, for a photon energy yielding $eKE = 50$ eV and at the magic angle.

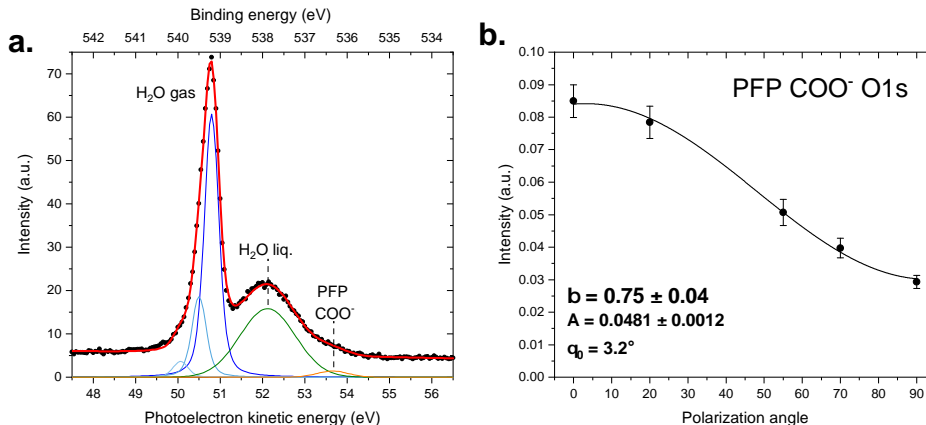


Figure S4: **a.** O 1s spectrum of a 100 mM NaPFP solution, measured at 590 eV photon energy ($eKE \sim 50$ eV) at the magic angle. All components of the spectrum are labeled in the panel. **b.** Measured PAD of the COO^- O 1s peak from panel a.

In the O 1s spectrum (Fig. S4a), the signature of the COO^- oxygen atoms appears as a shoulder at the low-binding-energy side of the liquid-water peak. Fitting constraints (fixed widths and relative positions) were used to ensure a proper extraction of the COO^- intensities, but the large overlap of the peaks adds to the uncertainty of the measurement. Note that the two oxygen atoms of the COO^- group are equivalent here, contrary to the case of the $COOH$ oxygen atoms of gas-phase PFPA presented in Fig. S1, which exhibits two distinct bands with different β parameters, also tabulated below in Table S1. The difference of gas-phase β value of the two non-equivalent $COOH$ oxygen atoms can be attributed to a difference of intramolecular scattering. For a comparison to the liquid COO^- oxygen atoms β values, we used the gas-phase β of the $C=O$ peak. Scattering occurs mostly on nuclei, and, therefore, the nascent anisotropy of the COO^- oxygen atoms PAD should be closer to that of the $C=O$ oxygen peak PAD.

1.3 Gas-phase β values and as-measured liquid β values

The measured values of β for gas-phase PFPA at different eKE are given in Table S1. Table S2 presents the as-measured β values for the 100 mM NaPFP solution that were used for Figs. 2 and 3 of the main text. Table S3 lists the results for three repeated experiments performed on different days and on two different beamlines at $eKE \sim 150$ eV. The β values match within error bars of ± 0.02 .

Table S1: Extracted β values for gas-phase PFPA at different eKEs.

	PFPA C 1s			PFPA O 1s	
	CF_3	CF_2	$COOH$	C-O-H	O=C
eKE ~ 50 eV	1.01 ± 0.005	1.03 ± 0.007	1.28 ± 0.017	1.69 ± 0.004	1.59 ± 0.004
eKE ~ 150 eV	1.66 ± 0.015	1.67 ± 0.027	1.73 ± 0.027		
eKE ~ 350 eV	1.79 ± 0.05	1.79 ± 0.05	1.82 ± 0.05		

1.4 Sensitivity limit of the measurements

In the main text, the sensitivity limit of our measurements, in the sense of what is the smallest distance between two (classes of) atoms that can be separated by comparing their R_β value, is discussed. The natural criterion for this distinction is that the error bars of two adjacent R_β values should not overlap. The error bars of the as-measured β values are determined from the fit result (see, e.g., Fig. S3). They typically vary between ± 0.01 and ± 0.04 . After error propagation, this results in errors for R_β between ± 0.04 and ± 0.06 , as mentioned in the main text.

Table S2: Liquid-phase β values before normalization for 100 mM NaPFP solution at different eKEs.

	PFPA C 1s				PFPA O 1s
	CF ₃	CF ₂	CF ₂ ^(COO⁻)	COO ⁻	COO ⁻
eKE \sim 50 eV	0.82 \pm 0.017	0.76 \pm 0.014	0.69 \pm 0.013	0.80 \pm 0.013	0.92 \pm 0.012
eKE \sim 150 eV	1.43 \pm 0.02	1.37 \pm 0.01	1.32 \pm 0.02	1.30 \pm 0.01	
eKE \sim 350 eV	1.75 \pm 0.04	1.68 \pm 0.05	1.60 \pm 0.06	1.62 \pm 0.05	

Table S3: β values from three repeated measurements across different days and measurement campaigns. NaPFP 100 mM PADs were measured at a photon energy to yield eKE \sim 150 eV at the C 1s edge. Experiment (1) was conducted at the PLEIADES beamline. Experiment (2) was conducted during the same beamtime, three days later, using a different batch of solution. Experiment (3) was conducted at the UE52_SGM beamline.

	PFPA C 1s			
	CF ₃	CF ₂	CF ₂ ^(COO⁻)	COO ⁻
Experiment (1)	1.44 \pm 0.015	1.38 \pm 0.01	1.32 \pm 0.02	1.31 \pm 0.02
Experiment (2)	1.42 \pm 0.018	1.36 \pm 0.009	1.32 \pm 0.03	1.29 \pm 0.01
Experiment (3)	1.42 \pm 0.02	1.38 \pm 0.015	1.32 \pm 0.015	1.30 \pm 0.018

Errors on the PE intensities, which are in turn carried over to errors on β values, have several possible origins aside from statistical fluctuations: First in the experimental measurement and the associated normalization procedures, and then in the evaluation of peak areas by fitting. For the latter, errors can be introduced by systematic bias present in the chosen fit constraints. This is difficult to quantitatively evaluate, but ‘hand-made’ estimates showed us that changing the fit constraints had little effect on the relative difference of β (within the error bars), while potentially introducing slight differences in the absolute values.

The most important source of experimental error is probably the change of alignment caused by slight variations in the jet position, which can hardly be avoided. This can be both caused by slow drifts over minutes or longer or abrupt position changes. Although this is partly accounted for by regularly checking the absolute count rate in the spectrum measured with vertical polarization and used as a reference, it remains most likely the most important source of error overall. In comparison, fluctuations of the photon flux and the associated detectors, of the order of 1% or less, are deemed negligible.

In order to get a better idea of the experimental reproducibility, we repeated a given experiment three times: Two measurements were done with three days of temporal distance and using a different batch of solution at the PLEIADES beamline, and a third one was carried out at the UE52_SGM beamline. The results are shown in Table S3 and show consistency within our error bars of the order of ± 0.02 .

2 Molecular dynamics simulations

2.1 Methods

A molecular dynamics (MD) simulation was conducted using the LAMMPS [4, 5, 6] package, version 29 Oct 2020. The SPC/Fw [7] model for water was used. OPLS-AA force fields (FFs) were generated using the LigParGen [8, 9] tool, with the exception of some torsional parameters, see section 2.2. CM5 charges [10] were calculated using the CM5-calculator [11], from Hirshfeld [12] charges based on a density functional theory (DFT) calculation at the globally optimized geometry. CM5 charges of chemically equivalent atoms were averaged. The PBE0 [13] exchange-correlation (xc) functional was used. The DFT calculation was done with FHI-aims [14, 15, 16, 17, 18], using its *really tight* default basis sets with additional `for_aux hydro 5 g 6.0` functions for all elements to increase the accuracy of the hybrid DFT calculation. Relativistic effects were treated by the scalar zeroth order regular approximation (ZORA) [14]. Van-der-Waals interactions were treated by the non-local many-body dispersion (MBD-NL) model in a post-SCF (self-consistent field) correction [19]. The ‘M’ parameter set of Ref. [20] was used for the Na⁺ ions.

The simulation cell had fixed lengths of 50 Å with periodic boundary conditions in x and y directions. In z direction, the cell was 210 Å long and periodic boundary conditions were only formally applied for the particle-particle-particle-mesh (PPPM) solver [22, 23], but corrected for to yield effectively open boundary conditions in that direction [5]. 8358 water molecules were placed in the cell, amounting to an approximately 100 Å thick slab. `fftool` [24] and `packmol` [25], version 20.2.2 were used in the creation of the water box. Aiming for a bulk concentration of 100 mM NaPFP, 15 PFP anions and 15 Na⁺ cations were inserted into the middle of the water slab. Aiming

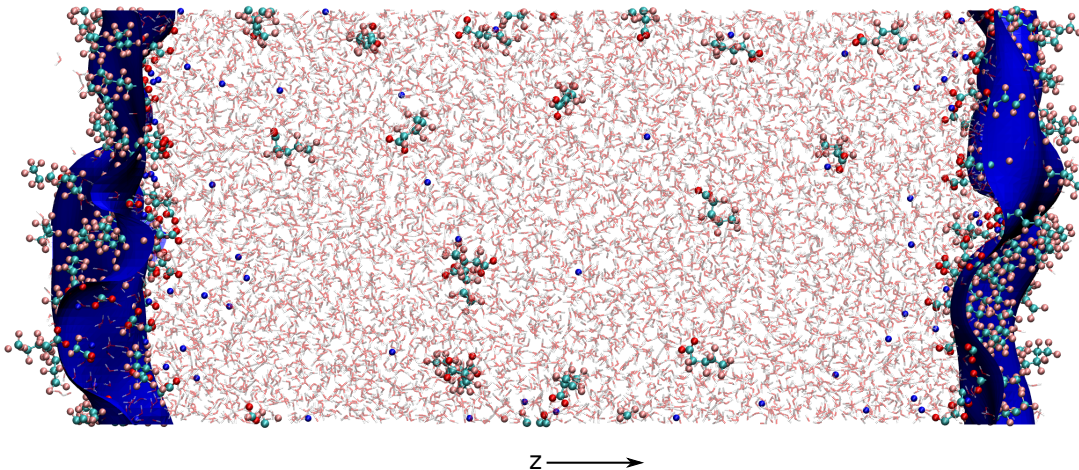


Figure S5: Snapshot from MD simulation. Na^+ shown in blue, C, O and F of PFP in teal, red and pink, respectively. Water molecules shown as transparent wedges. Instantaneous interfaces [21] shown as solid blue surfaces. One simulation cell is shown here. Periodic boundary conditions are applied in x and y directions to form a water slab.

for a surface coverage of $2.0 \cdot 10^{14} \text{ cm}^{-2}$, 50 such pairs were placed above the water slab, and 50 below it. This surface coverage corresponds to a rough estimate of the experimental surface coverage, based on surface tension measurements. One unit cell of the system after equilibration is shown in fig. S5.

Lennard-Jones walls were placed 5 \AA above the lower and below the upper cell boundary to prevent molecules from leaving the simulation cell [5]. The used FFs underestimate the surface coverage to bulk concentration ratio of NaPFP. This was corrected by adjusting the chemical potential with a z -dependent bias potential as described in section 2.3.

The MD simulations were conducted in the NVT ensemble by applying a Nosé-Hoover thermostat [26, 27] with fixed cell dimensions at 300 K. Drift of the water box as a whole in z direction was prevented by subtracting the center-of-mass velocity from the velocities of all atoms in each time step and re-scaling the velocities to conserve kinetic energy [5]. Time steps of 1 fs were used. All systems were equilibrated for $2 \cdot 10^6$ time steps before running $2 \cdot 10^7$ time steps of production calculation. For evaluation, every 2000th MD step of the latter was used as a snapshot.

For the final analysis and comparison to our experimental data, distributions of the C and O atoms along the z axis (i.e. the global surface normal) were determined relative to the instantaneous surface of the polar phase in the fashion of Ref. [21]. The polar phase was defined by Na and O atoms, including those of PFP. A coarse-graining length of $\xi = 3.16 \text{ \AA}$ was chosen and the density isovalue for the interface was chosen to be half the maximum density in the bulk. The resulting instantaneous interface is illustrated in fig. S5, and the vertical distributions are shown in fig. S6.

2.2 Force-field parameterization

Torsional parameters for fluorinated molecules are not generally available in the OPLS-AA FF. For the F-CT-CT-F and CT-CT-CT-F torsions, we employ the parameters from Ref. [28]. For the remaining torsions, we developed our own set of parameters, retaining the functional form of OPLS-AA.

$$E(\theta) = \frac{1}{2} (V_1(1 + \cos(\theta)) + V_2(1 - \cos(2\theta)) + V_3(1 + \cos(3\theta)) - V_4(1 - \cos(4\theta))) \quad (2)$$

Here, E is the energy contribution of a torsion, θ is the corresponding dihedral angle, and V_1 to V_4 are the to-be-determined parameters. In principle, the torsions without readily available parameters are: CT-CT-CT-CT, CT-

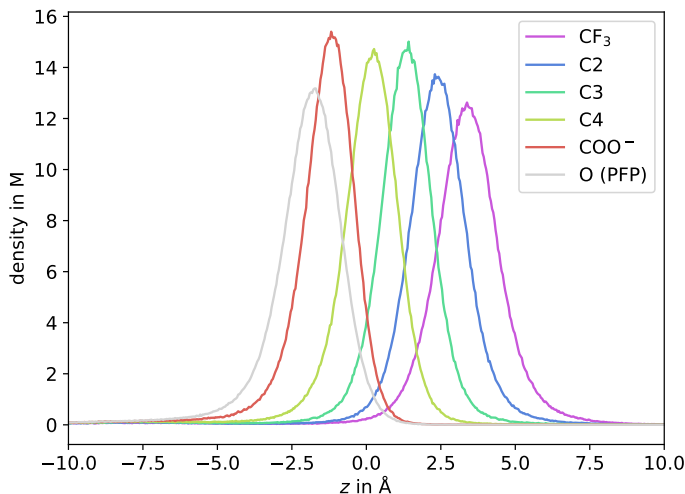


Figure S6: Vertical distributions of the C and O atoms of PFP relative to the instantaneous water surface in the MD simulation. Broader distributions towards the CF_3 end of the chain represent a higher vertical thermal mobility relative to the water surface.

CT-CT-C(=O), F-CT-CT-C(=O), F-CT-C=O, and CT-CT-C=O. However, CT-CT-C=O describes functionally the same torsion as F-CT-C=O, up to distortions in the tetrahedral coordination of the CT atom. The same can be said about CT-CT-CT-C(=O) and F-CT-CT-C(=O).

Therefore, three series of reference calculations were conducted in FHI-aims, using the same methods as described in the previous section. In each series, the corresponding dihedral angle (CT-CT-CT-CT, CT-CT-CT-C(=O), and CT-CT-C=O) was scanned in steps of 10° , starting at 180° . At each step, the molecular geometry was optimized, constraining the respective dihedral at the desired value. As an initial guess for geometry optimization, the optimized geometry from the previous step was used, with the dihedral adapted accordingly. Despite the molecule's symmetry, this scan was done over full 360° , to compensate for hysteresis in the geometries. The Atomic Simulation Environment ASE [29] was used for the constrained relaxation. Forces and energies for the relaxation were calculated with the *tight* default basis sets of FHI-aims with additional `for_aux hydro 5 g 6.0` functions. The energy of the optimized geometry was finally re-calculated using the basis described in the previous section.

OPLS-AA torsional parameters were fitted to the such obtained reference. In the present work, we are interested in equilibrium properties, but not in kinetics. Therefore, conformations with lower energy were given higher weights in the fitting than those with higher energy. Specifically, the following procedure was employed:

1. Conformation i , characterized by the respective dihedral angle θ_i , with DFT reference energy E_i^{ref} was given a raw weight $w_i^{\text{ref}} = \exp(-E_i^{\text{ref}}/k_{\text{B}}T)$ with the Boltzmann constant k_{B} and the temperature $T = 300$ K. For each series, the weights were then normalized according to $\tilde{w}_i^{\text{ref}} = w_i^{\text{ref}} / \sum_j (w_j^{\text{ref}})$. Each conformer was given an initial weight $\tilde{w}_i = \tilde{w}_i^{\text{ref}}$.
2. Force-field parameters were calculated to minimize the error $p = \|\mathbf{E}^{\text{ref}} - \mathbf{E}^{\text{FF}}\|$ with the vectors $\mathbf{E}^{\text{ref/FF}}$ containing the reference / force-field energies of all three series combined, weighted by \tilde{w}_i . Force-field energies were calculated at the reference geometries. The weights of the CT-CT-C=O series were halved to account for symmetry. Since only energy differences are meaningful in classical FFs, one constant offset for each series was included in the fitting.
3. So far, this enforces that minima of the reference energy are reproduced well. However, additional minima of the force-field energy might exist elsewhere, which will also skew equilibrium distributions. Therefore, additional weights w_i^{FF} were calculated from the force-field energies and normalized in complete analogy to step 1. Each conformer was then given the averaged weight $\tilde{w}_i = 1/2 \cdot (\tilde{w}_i^{\text{ref}} + \tilde{w}_i^{\text{FF}})$.
4. Steps 2 and 3 were repeated to self-consistency.

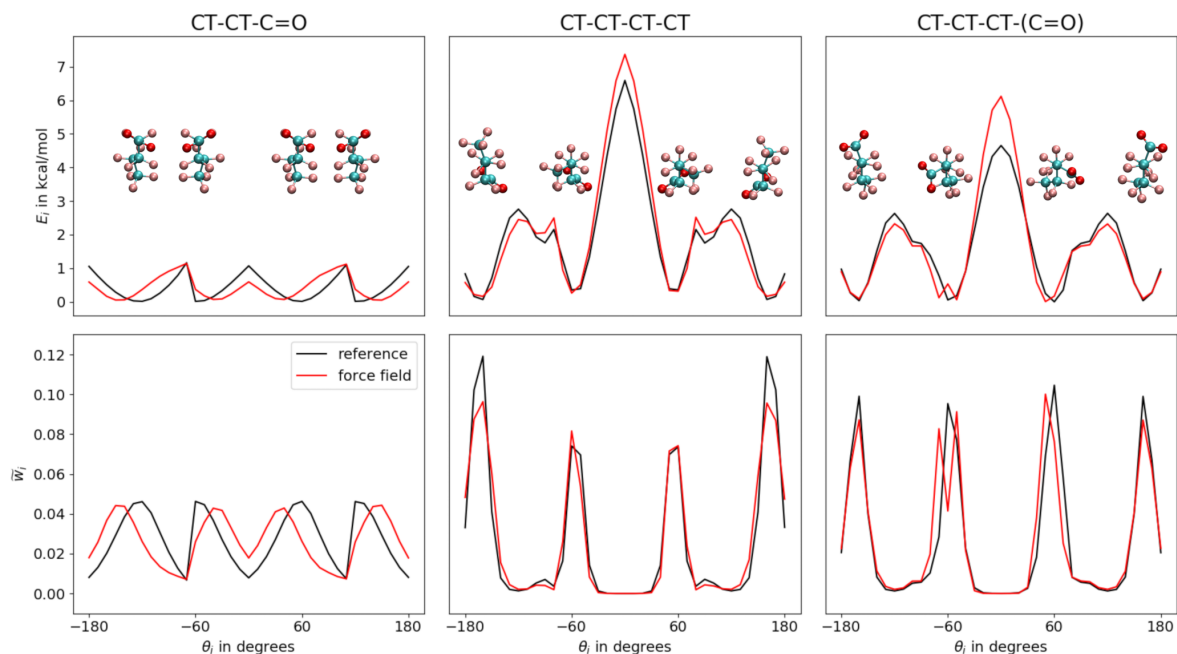


Figure S7: Energy profiles (top) and estimated thermal distributions (bottom) of the three torsions in PFP for which new OPLS-AA parameters were determined in this work (the first series scanned CT-CT-C=O in steps of 10° , but describing practically the same torsion by F-CT-C=O in the force-field energy turned out to yield a slightly smaller error). Geometries corresponding to the local minima of the reference energy shown as insets.

We introduce a second error function $p_2 = \|\tilde{\mathbf{w}}^{\text{ref}} - \tilde{\mathbf{w}}^{\text{FF}}\|$. Here, the vectors $\tilde{\mathbf{w}}^{\text{ref/FF}}$ contain $\tilde{w}_i^{\text{ref/FF}}$ of one of the three series. Since nuclear degrees of freedom except the three dihedral angles were optimized rather than thermodynamically sampled, p_2 gives only an estimate rather than an exact measure for the error in the thermal distributions.

The above procedure was re-iterated multiple times to avoid overfitting:

1. In the first fit, all terms of all 5 torsions were fitted freely, with the exception of the $\cos(\theta)$ and $\cos(3\theta)$ terms in the F-CT-C=O and CT-CT-C=O torsions, which would cancel due to symmetry. This produces large coefficients, indicating heavy overfitting; but it gives a lower bound on the errors p_2 that can be achieved within this model.
2. The highest of the coefficients was found (V_1 of the CT-CT-CT-C(=O) torsion) and its redundant counterpart (V_1 of F-CT-CT-C(=O)) identified. It was tested the removal of which of the two terms results in a smaller $\max(p_2)$ after re-fitting, with the maximum taken over the three series. From the resulting parameters, the highest one was found again and the procedure repeated, until no redundant pairs of parameters were left. This leaves us with 10 parameters: V_2 and V_4 of F-CT-C=O, and V_1 to V_4 of CT-CT-CT-CT and of CT-CT-CT-C(=O).
3. For each remaining term, it was tested if it can be removed without a significant increase in p or $\max(p_2)$. This was the case for V_2 of CT-CT-CT-CT.
4. Lastly, L_2 regularization [30] was applied to reduce overfitting. The regularization strength was chosen as high as possible without significantly changing the thermal distributions between the *gauche* and (distorted) *anti* conformers of the two C-C-C-C torsions.

The final parameters are summarized in table S4, and the torsional profiles shown in fig. S7.

Table S4: OPLS-AA torsional parameters for PFP determined in this work, in kcal/mol.

	F-CT-C=O	CT-CT-CT-CT	CT-CT-CT-C(=O)
V_1	0	4.981	5.453
V_2	-0.804	0	-0.765
V_3	0	-2.062	-0.662
V_4	0.221	-0.986	-1.026

2.3 Bias potential

Running an MD simulation as described in section 2.1, but without the bias potential which will be discussed in this section leads to a significant portion of NaPFP diffusing from the water surface into bulk water. As seen in fig. S8(a), surface and bulk PFP can be clearly distinguished in the vertical distributions of the C atoms. For each C atom, the surface can be defined to begin at its concentration minimum.

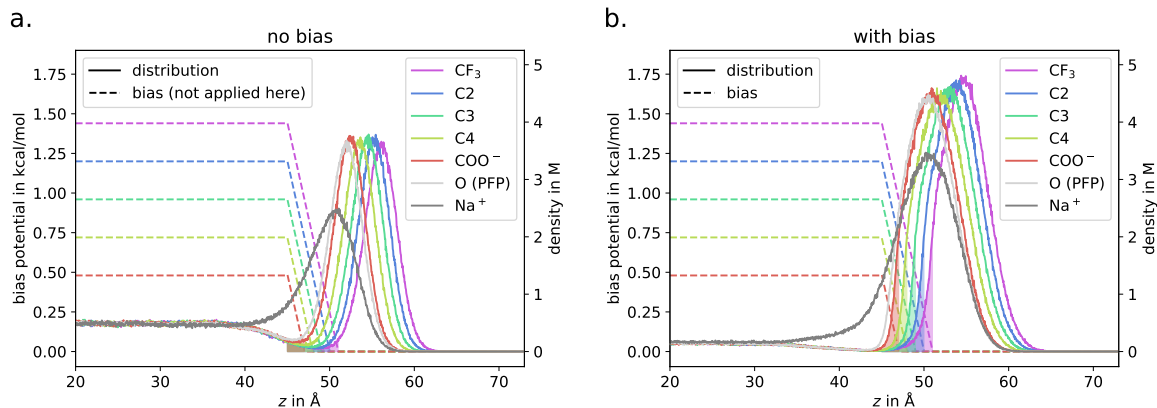


Figure S8: Vertical distributions of the different C atoms, as well as Na⁺ and the O atoms of PFP with respect to the center of the water slab in the MD simulations. Data from upper and lower surface averaged. **a.** Without bias potential applied; bias shown only for reference. **b.** With bias potential. Shaded areas indicate the portion of C atoms which experience (or would experience, in the case of **a.**) a force from the bias potential.

To quantify the surface coverage, the peak of the CF₃ carbon atom, which shows the most pronounced minimum between bulk and surface, is integrated. All PFP anions which are not assigned to the surface in this way are assigned to the bulk. We further assume that the volume V and surface area A of our model system are exactly as in the initial geometry, i.e. $A = (50 \text{ \AA})^2$ and $V = A \cdot 100 \text{ \AA}$. With this information, we calculate a surface coverage of $1.08 \cdot 10^{14} \text{ cm}^{-2}$, and a bulk concentration of 405 mM.

The error can be expressed in terms of an error in the chemical potential difference $\Delta\gamma$ between surface and bulk. The order of magnitude of this error can be estimated by assuming

$$\frac{\sigma(\text{Na}^+)\sigma(\text{PFP}^-)}{\rho(\text{Na}^+)\rho(\text{PFP}^-)} \sim \exp\left(-\frac{\Delta\gamma}{k_B T}\right) \quad (3)$$

with the surface coverages σ and bulk concentrations ρ of Na⁺ and PFP. The values for PFP are obtained as described above, and we assume $\sigma(\text{Na}^+) = \sigma(\text{PFP}^-)$ and $\rho(\text{Na}^+) = \rho(\text{PFP}^-)$ for reasons of charge neutrality. With the values reported above, this leads to an estimated error in $\Delta\gamma$ of 2.4 kcal/mol.

With Na⁺ known to be generally well soluble in water, we assume that the error in $\Delta\gamma$ originates from the PFP FF. We consequently apply a bias potential to the PFP anions, specifically to their C atoms. Ideally, we want the bias forces to act only in the transition region between bulk and surface, with constant bias potentials in both regions. Bias forces acting in the surface region would skew the property in which we are ultimately interested, i.e. the structure of the surfactant layer. In contrast, bias forces acting in the bulk would generate an unphysical

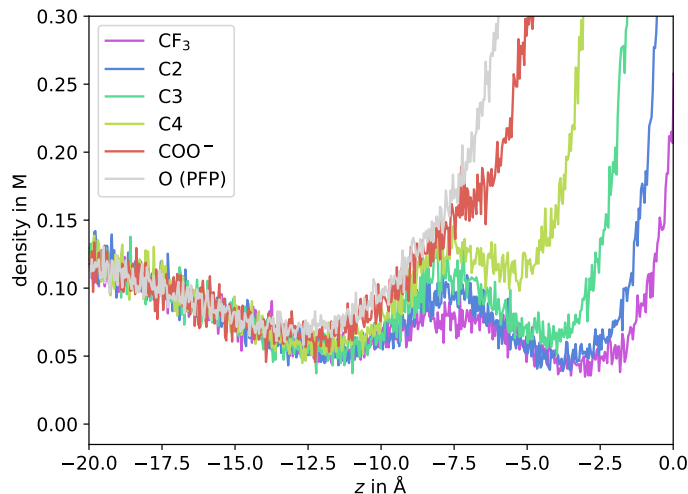


Figure S9: Vertical distributions of the C and O atoms of PFP relative to the instantaneous water surface with bias applied, in the transition region between bulk and surface.

sub-surface region with lower chemical potential than the bulk where PFP would accumulate, potentially perturbing the surfactant structure as well.

We choose a bias force which is constant [5] within the respective regions where it applies, and equal for all C atoms. For the carboxylic C atom, this force is applied in the region between 45 Å and 47 Å from the center of the water slab. For each further C atom along the chain, the upper limit was increased by 1 Å while the lower limit was kept fixed, as shown in fig. S8. The magnitude of the bias force was chosen such that the resulting potentials in the bulk sum up to the desired correction to $\Delta\gamma$. By systematic testing we find that the bias actually needs to be higher than the estimated 2.4 kcal/mol. At 4.8 kcal/mol, we achieve $\sigma(\text{PFP}^-) = 1.96 \cdot 10^{14} \text{ cm}^{-2}$.

This results in an acceptable compromise between keeping the surface layer free from bias forces and preventing the formation of an unphysical sub-surface layer. Only 6.1 % of the CF_3 carbons in the surface layer actively experience the bias force, and the fraction is smaller for the other C atoms. On the other hand, a fluctuation in the distributions relative to the instantaneous water surface is observed below the surface layer, but it is small as seen in fig. S9.

3 Validity of the β linearity

Equation 2 in the main text was derived from an analytical approximation of the differential scattering cross section (DCS) for elastic scattering by a Gaussian. This implies a number of limitations. Realistic DCS are more complex and for electron energies below 100 eV include a non-negligible backscattering component. As pointed out by Schild et al. [31], the convolution formula used here is only one-dimensional, whereas it would be more correct to use a two-dimensional convolution in spherical coordinates. To test the influence on the behavior of the scattered β^* relative to the initial β , we numerically computed the n -fold convolution of an initial PAD with more realistic DCS. Only calculated DCS are used here, as the available experimental DCS, e.g. for gas phase water [32], do not measure the forward scattering component (close to 0°) which is in fact the most intense component by far. DCS curves for electron energies of 100 and 400 eV were extracted from the NIST electron elastic-scattering cross-sections database [33] using a model of water consisting of simply elemental oxygen and hydrogen. For comparison, the DCS calculated by Schild et al. [31] for a 7-water cluster model is shown, which was assumed by the authors to converge sufficiently towards bulk water behavior. These DCS are plotted in Fig. S10a. We also computed the 2D convolution of the PAD with the simple Gaussian DCS, using the formula given in Ref. [31].

The resulting β^* as a function of the number of elastic scattering events n is displayed in Fig. S10b. All curves were fitted using Eq. 2 from the main text. One can observe that all one-dimensional convolutions are perfectly fitted by Eq. 1, with only the effective value of ϕ changing. This formula seems to be valid no matter what the

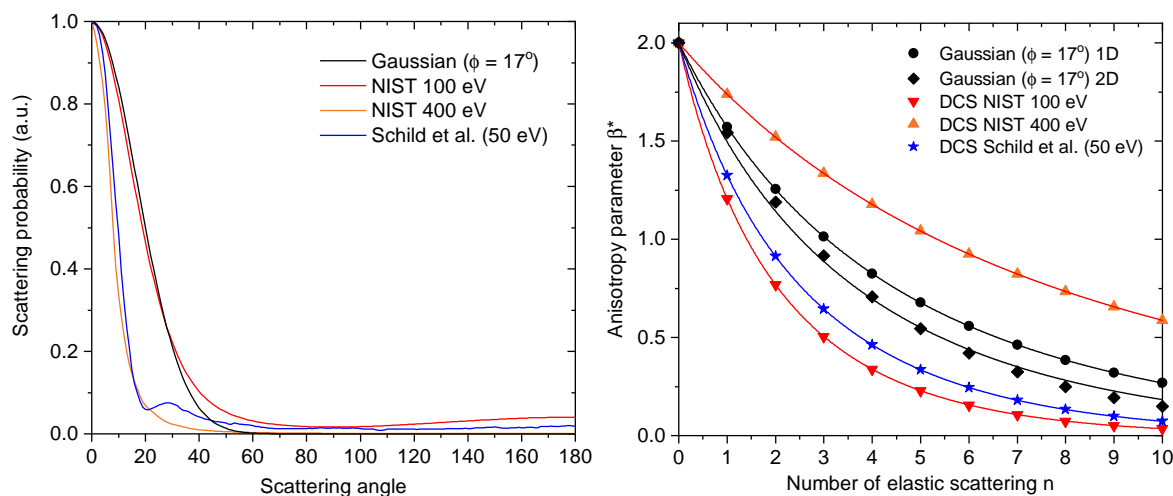


Figure S10: **a.** Exemplary differential cross sections for elastic scattering, which were used to compute the data from panel b. References are given in the text. **b.** Computed anisotropy parameter β^* of the distribution obtained after n -fold convolutions of various DCS with an initial PAD with $\beta = 2$.

exact shape of the DCS is. For the two-dimensional convolution, some discrepancies can be observed, but the equation can still reproduce fairly well the curve, with a slightly different effective ϕ than the one of the initial Gaussian. Schild et al. [31] also pointed out the potential importance of surface effects in the simulation of angular distributions. The surface, however, would not influence the linearity of the β scale with depth.

In conclusion, linearity is always expected for low- n regimes no matter what the shape of the DCS is. Only the regime of validity of the low- n approximation changes. Since the appropriate DCS for our experiments is not easily accessible and other effects may come into play, we refrain from interpreting the absolute value of the slope.

References

- [1] R. Dupuy *et al.*, Phys. Chem. Chem. Phys. **24**, 4796 (2022).
- [2] T. Lewis *et al.*, J. Phys. Chem. C **123**, 8160 (2019).
- [3] S. Thürmer *et al.*, Phys. Rev. Lett. **111**, 173005 (2013).
- [4] S. Plimpton, J. Comput. Phys. **117**, 1 (1995).
- [5] S. Plimpton, A. Kohlmeyer, A. Thompson, S. Moore, and R. Berger, LAMMPS Stable release 29 September 2021 (stable_29Sep2021_update3). Zenodo., 2020.
- [6] A. P. Thompson *et al.*, Comput. Phys. Commun. **271**, 108171 (2022).
- [7] Y. Wu, H. L. Tepper, and G. A. Voth, J. Chem. Phys. **124**, 024503 (2006).
- [8] W. L. Jorgensen and J. Tirado-Rives, Proc. Natl. Acad. Sci. U.S.A. **102**, 6665 (2005).
- [9] L. S. Dodda, I. Cabeza de Vaca, J. Tirado-Rives, and W. L. Jorgensen, Nucleic Acids Res. **45**, W331 (2017).
- [10] A. V. Marenich, S. V. Jerome, C. J. Cramer, and D. G. Truhlar, J. Chem. Theory Comput. **8**, 527 (2012).
- [11] P. Melix, patrickmelix/cm5-calculator: First Production Release (v1.0), 2019.
- [12] F. L. Hirshfeld, Theor. Chim. Acta **44**, 129 (1977).
- [13] C. Adamo and V. Barone, J. Chem. Phys. **110**, 6158 (1999).

- [14] V. Blum *et al.*, *Comput. Phys. Commun.* **180**, 2175 (2009).
- [15] X. Ren *et al.*, *New J. Phys.* **14**, 053020 (2012).
- [16] V. W. Yu *et al.*, *Comput. Phys. Commun.* **222**, 267 (2018).
- [17] V. Havu, V. Blum, P. Havu, and M. Scheffler, *J. Comput. Phys.* **228**, 8367 (2009).
- [18] A. C. Ihrig *et al.*, *New J. Phys.* **17**, 093020 (2015).
- [19] J. Hermann and A. Tkatchenko, *Phys. Rev. Lett.* **124**, 146401 (2020).
- [20] M. M. Reif and P. H. Hünenberger, *J. Chem. Phys.* **134**, 144104 (2011).
- [21] Z. Liu, T. Stecher, H. Oberhofer, K. Reuter, and C. Scheurer, *Mol. Phys.* **116**, 3409 (2018).
- [22] R. W. Hockney and J. W. Eastwood, *Computer Simulation Using Particles* (Routledge; Special Student ed., 1988).
- [23] R. E. Isele-Holder, W. Mitchell, and A. E. Ismail, *J. Chem. Phys.* **137**, 174107 (2012).
- [24] A. Padua, *agiliopadua/fftool: Update (v1.1)*. Zenodo., 2019.
- [25] L. Martínez, R. Andrade, E. G. Birgin, and J. M. Martínez, *J. Comput. Chem.* **30**, 2157 (2009).
- [26] S. Nosé, *J. Chem. Phys.* **81**, 511 (1984).
- [27] W. G. Hoover, *Phys. Rev. A* **31**, 1695 (1985).
- [28] E. K. Watkins and W. L. Jorgensen, *J. Phys. Chem. A* **105**, 4118 (2001).
- [29] A. H. Larsen *et al.*, *J. Phys.: Condens. Matter* **29**, 273002 (2017).
- [30] A. Y. Ng, Feature selection, L1 vs. L2 regularization, and rotational invariance, in *Proceedings of the Twenty-First International Conference on Machine Learning, ICML '04*, p. 78, New York, NY, USA, 2004, Association for Computing Machinery.
- [31] A. Schild, M. Peper, C. Perry, D. Rattenbacher, and H. J. Wörner, *J. Phys. Chem. Lett.* **11**, 1128 (2020).
- [32] M. A. Khakoo *et al.*, *Phys. Rev. A* **78**, 052710 (2008).
- [33] A. Jablonski, F. Salvat, C. J. Powell, and A. Y. Lee, *NIST Electron Elastic-Scattering Cross-Section Database Version 4.0, NIST Standard Reference Database Number 64* (National Institute of Standards and Technology, Gaithersburg, MD, 2016).